Available online at www.sciencedirect.com

ScienceDirect

journal homepage: www.elsevier.com/locate/he

Organic molecule-functionalized Zn_3P_2 nanowires for photochemical H_2 production: DFT and experimental analyses

G. Ramos-Sanchez [a], M. Albornoz [a], Y.-H. Yu [d], Z. Cheng [a,d], V. Vasiraju [d], S. Vaddiraju [a,d], F. El Mellouhi [b,c], P.B. Balbuena [a,d,*]

[a] Artie McFerrin Department of Chemical Engineering, Texas A&M University, College Station, TX 77843, USA
[b] Physics Department, Texas A&M University at Qatar, Texas A&M Engineering Building, Education City, Doha, Qatar
[c] Qatar Energy and Environment Research Institute, P.O. Box 5825, Doha, Qatar
[d] Department of Materials Science & Engineering, Texas A&M University, College Station, TX 77843, USA

ARTICLE INFO

Article history:
Received 3 May 2014
Received in revised form
1 October 2014
Accepted 6 October 2014
Available online 31 October 2014

Keywords:
Hydrogen production
Density functional theory
Photochemical reactions
Zinc sulfide
Electron transfer
Functionalized nanowires

ABSTRACT

Hydrogen production via photochemical reactions in water/methanol solutions containing Zn_3P_2 nanowires functionalized with an organic molecular layer is shown to be between 217 and 405 times higher than that obtained in absence of the molecular layer. Combined surface characterization and theoretical analyses are used to elucidate aspects of the photochemical reaction process. It is found that the protective layer exerts a passivation role decreasing the rate of nanowire degradation, while facilitating electron transfer for the hydrogen evolution reaction.

Introduction

Harvesting solar energy has for a long time been one of the dearest dreams of mankind due to the desire of having an abundant, cheap, continuous and nearly infinite energy supply. Solar-driven hydrogen generation has been recognized as a green and promising way of producing clean energy providing an alternative to solving the fossil fuel shortage problems. Water and sunlight are renewable and cheap resources thus increasing the relevance and feasibility of these processes. As discussed by Lewis [1], the conversion of solar energy into a usable energy source is possible by using nanoparticle-based photochemical water splitting systems. The main requirements for production of hydrogen via water splitting are: 1) Adequate electronic structure to absorb photons and producing excited electrons; 2) The electron and hole must be separated to avoid recombination; and 3) The excited

* *Corresponding author*. Artie McFerrin Department of Chemical Engineering, Texas A&M University, College Station, TX 77843, USA.
E-mail address: balbuena@tamu.edu (P.B. Balbuena).
http://dx.doi.org/10.1016/j.ijhydene.2014.10.028

electron should be able to undergo the desired chemical reactions. Most semiconducting materials are able to absorb light efficiently and perform electron–hole separation; however most of them have large band gap and absorbing wavelength in the UV region. Since the first report of water splitting using TiO_2 [2], many materials have been used, among them $SrTiO_3$, $KTaO_3$, ZnO and ZnS [3], but these materials absorb in the UV region which is 5% of the solar spectrum. In order to have a highly efficient system, materials that absorb in the visible region are preferred. This is because 49% of the solar energy radiation that continuously reaches the earth is within the visible spectrum 400–750 nm [4], while 5% of this radiation has a wavelength below 400 nm (UV). From the calculated position of conduction and valence bands for different oxides and sulfides it becomes apparent that most of metallic oxides have large band gaps while the sulfides possess narrower band gaps leading to a higher absorption of sunlight. However, sulfide materials are less stable and are prone to undergo photochemically or chemically assisted oxidation reactions. Therefore, a new requirement is added to the three above mentioned: screening materials featuring long term stability combined with adequate band gap to absorb in the visible region. Unfortunately, materials that are stable in water and can split water into H_2 and O_2 do not absorb sunlight effectively, and the materials that absorb sunlight effectively cannot sustain photochemically induced water-splitting [1].

The optical properties and band structure of Zn_3P_2 have been studied extensively; the results indicate that the electronic structure of the solid phase is appropriate for photochemical water splitting [5–7]. Moreover, this compound has one of the highest potentials for energy production and is the least expensive among 23 different compounds evaluated, therefore making it one of the best candidates for solar water splitting [8]. Unfortunately, it suffers of poor stability [9] leading to the dissolution of Zn and to the complete loss of its photochemical properties. Recently, a novel vapor phase method for the synthesis of gram quantities leading to high quality Zn_3P_2 nanowires was reported [10]. Moreover, Zn_3P_2 nanowires were fabricated using the same method and a one-step functionalization process was carried out by exposing the nanowires directly to a vapor of organic functional molecules immediately after their synthesis. This functionalization offers the advantage of passivating the surfaces, making them resistant against air and moisture-assisted degradation. These functionalized nanowires demonstrated an enhanced degradation resistance up to 120 days in THF solvent [11].

Ideally, water splitting is initiated by the absorption from a light source of an energy equal to or larger than the bandgap of the functionalized nanowires. This process leads to the creation of free electrons and holes within the nanowires. The photogenerated electrons may reduce H^+ to H_2 while the holes may oxidize H_2O becoming the source of H^+ [12]. However, it is known that direct splitting of water into hydrogen and oxygen is hindered due to fast and thermodynamically favorable electron–hole recombination [13]. A strong reducing agent (electron donor), such as methanol, is often used as hole scavenger to mitigate undesired electron–hole recombination reaction. The process is shown in Fig. 1.

The hypotheses behind the schematic process presented in Fig. 1 are as follows: a) The use of semiconductors with nanowire morphology will facilitate the increase of the interfacial area where photons may accomplish the first step of electron–hole production; b) the band-gap of the semiconductor can be tuned by adsorbing a suitable molecular monolayer, which also serves as an inhibitor for dissolution reactions and also acts as an electron transfer medium; c) the oxidation of a proper additive (methanol) will allow generation of protons which will be reduced by the generated electrons to produce molecular hydrogen.

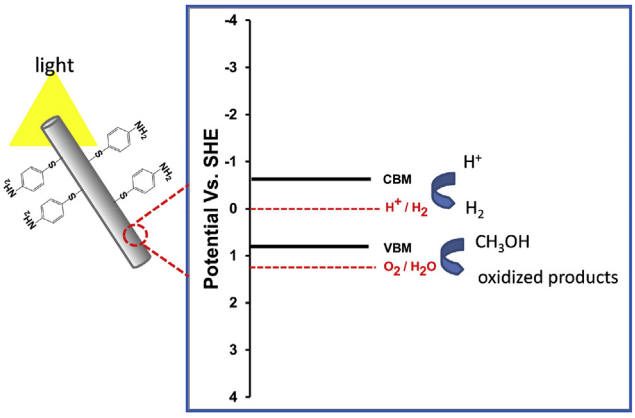

Fig. 1 – Schematic illustration of the process involving Zn_3P_2 nanowires and proposed interfacial reactions.

In order to explain the changes induced by the functionalization process and the subsequent induced charge transfer characteristics, density functional theory (DFT) calculations are performed to characterize the bulk, surface, and functionalized Zn_3P_2 systems. In the first part of this paper, the characteristics of bulk Zn_3P_2 and of the (100) Zn_3P_2 surface are analyzed along with adsorption properties of two organic molecules 4-aminothiophenol (4-ATP) and 1,3 propanedithiol (1,3-PDT). These molecules were selected on the basis of previous experiments carried out on Zn_3P_2 nanowires indicating good protective properties [11]. Next, experimental results of photocatalytic hydrogen production are presented and discussed based on photochemical reactions of water–methanol mixtures on Zn_3P_2 nanowires coated with 4-ATP and 1,3-PDT. The full analysis and theoretical–experimental approach is intended to serve as a landmark for future explorations of alternative organic coatings for achieving improved stability and catalytic activity. Finally, a preliminary theoretical analysis of the interactions of the coating molecules with a silver atom is conducted to provide insights into the role of co-catalysts and their possible influence on hydrogen production.

Materials and methods

Computational details

The DFT calculations were performed using the Vienna ab initio Software Package, VASP [14,15]. Two functionals were used: the generalized gradient approximation (GGA) with the Perdew–Burke–Ernzerhof [16] (PBE) functional and the screened hybrid functional of Heyd–Scuseria–Ernzerhof

HSE06 [17,18] with its original parameterization (0.25 portion of exact exchange with a screening parameter of 0.20 $Å^{-1}$). Basis functions were constructed using the Projector Augmented Wave (PAW) method for the valence electrons, while ultra-soft pseudopotentials were used to represent core electrons [19,20]. In all cases the planewave cut off energy was optimized and set equal to 400 eV, and the total energy was calculated with the tetrahedron method with Blöchl corrections. The irreducible Brillouin zone (IBZ) was sampled with a Monkhorst–Pack grid of $4 \times 4 \times 4$ k-points [21] for the bulk and $4 \times 4 \times 1$ for the slab calculations. For the calculation of electronic density of states (DOS) of Zn_3P_2, the k-point meshes were kept to $4 \times 4 \times 4$ because of the high computational demand of the HSE06 functional. Ground state energies and charge densities were calculated self-consistently using blocked Davidson minimization algorithm. Initial charge densities were taken as a superposition of atomic charge densities. Atomic positions were relaxed to their ground state by minimizing their Hellman–Feynman forces.

Additional calculations were performed using the Gaussian suite [22], with periodic boundary conditions [23,24]. The Def2- [25] series of Gaussian basis sets were optimized following the procedure in Ref. [26], for the atomic species of interest in this work. Most numerical settings in Gaussian were left at the default values, geometry optimization settings, integral cut-offs, and self-consistent convergence thresholds. The default k-point mesh of $6 \times 4 \times 2$ was used for the slab calculations.

Experimental details

Zn_3P_2 nanowires morphologies were prepared as described in Ref. [11] and characterized by scanning electron microscopy (SEM, Quanta 600). Photocatalytic hydrogen production was carried out in a 250 mL pyrex round bottom flask, irradiating with a 500 W of high pressure mercury lamp equipped with a cut-off filter (Hoya, L42) and the system was maintained at room temperature by circulation of cooling water. A Zn_3P_2 nanowire foil was firstly cut into a 1 cm $\times$ 4 cm piece and then put into 150 mL of water–methanol (20% V/V) aqueous solution. The system was degassed with N_2 gas for 30min before irradiation. The amount of produced hydrogen was analyzed by gas chromatography (GC, Agilent 7820A) with a TCD detector equipped with a 5 Å molecular sieve column. The weights of Zn_3P_2 nanowires were determined by removing the Zn_3P_2 nanowires from the foil and measuring the weight difference.

Results and discussion

DFT analysis of bulk Zn_3P_2

The bulk Zn_3P_2 unit cell contains 40 atoms arranged in a rather complicated structure as shown in Fig. 2. Zn atoms are present in two coordination modes: tri- and tetra-coordinated, while P atoms appear in hexa- and tetra-coordinated arrangements. Bulk lattice parameters and interatomic bond distances and angles obtained from fully relaxed structures using PBE and HSE06 xc-functionals are presented in Table 1 and compared to experimental values [27,28]; the comparison of lattice parameters shows good agreement.

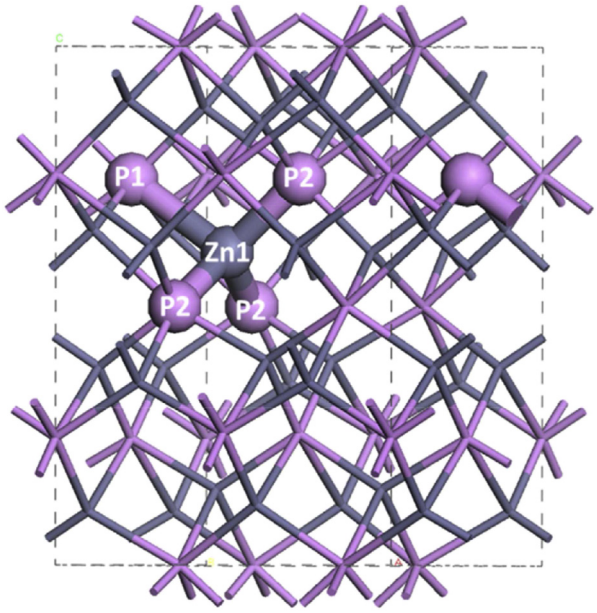

Fig. 2 – Geometry of bulk Zn_3P_2 unit cell. Dotted lines represent the supercell while gray and pink represent Zn and P atoms respectively. Atoms discussed in Table 1 are labeled and highlighted with larger spheres. (For interpretation of the references to color in this figure legend, the reader is referred to the web version of this article.)

Along with cell parameters, Zn_1, P_1 and P_2 atoms are depicted in Fig. 2. These atoms were chosen to illustrate representative distances among the largest and shortest bonds in Zn_3P_2 respectively. With respect to the selected P_2 atoms although they are not completely equivalent (differences in coordination), the average distance Zn_1-P_2 shown in Table 1 provides an estimate of the differences yielded by the two computational methods with respect to the experimental results. The results indicate that both functionals are able to accurately represent the bulk phase geometry. However, the resulting electronic structures obtained from each functional are very different. Fig. 3 shows the calculated projected density of states (PDOS) of the bulk system. Both PBE and HSE06 functionals give very similar characteristics of the valence band (VB), while differences appear in the band gaps and states of the conduction band (CB). The PDOS obtained by

Table 1 – Calculated lattice parameters (*a*, *b*, *c*) and interatomic distances of the bulk Zn_3P_2 unit cell compared to experiment. Zn_1, P_1 and P_2 atoms are depicted in Fig. 1.

	HSE06	PBE	Exp [27]
a, *b*/Å	8.103	8.111	8.078
c/Å	11.421	11.447	11.396
Zn_1–P_1	2.812	2.804	2.770
Zn_1–P_2	2.400	2.402	2.442

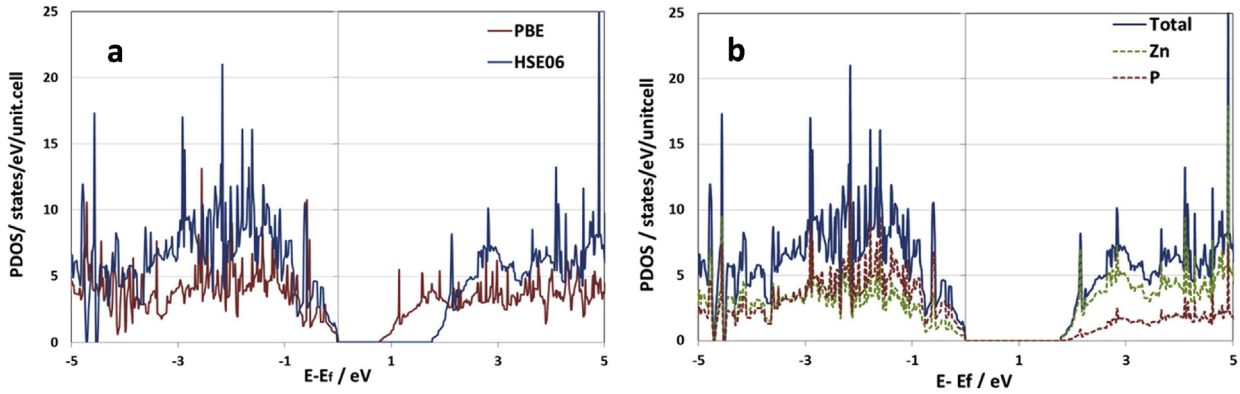

Fig. 3 – Projected electronic DOS of bulk Zn_3P_2 obtained by DFT calculations. (a) Comparison of PDOS for the functionals shown in the legend. (b) Projected DOS calculated with the HSE06 XC functional. Energies are relative to the Fermi level (E_F).

HSE06 XC functional depicted in Fig. 3b shows a better representation of the electronic structure in comparison with previous reports [6]. The calculated band gap of 1.7 eV is very close to the experimental value (1.6 eV) [7]. The VB states are a result of hybridization of Zn and P states with a higher contribution of the P atom states. Upon photoexcitation, an electron will migrate from the valence band to the conduction band (Zn atoms) leaving behind a hole at the valence band.

DFT evaluation of the Zn_3P_2 (100) surface

Experimentally, Zn_3P_2 nanowires are fabricated by transferring P onto heated zinc foils leading to the formation of nanowires of 30–50 nm in diameter and approximately ~10 μm long. The nanowires are single crystalline and grow along the [101] direction; therefore nanowire surfaces can be represented by a (100) slab. For the computational analysis four Zn_3P_2 slabs were built starting from the bulk optimized structure. Each slab is composed of five atomic layers separated with a 20 Å vacuum, each layer is composed by 10 atoms: 6 Zn and 4P. The slab thickness was determined on the basis of the bulk unit cell composed of four atomic layers each having a slightly different bonding pattern (see Fig. 2). Therefore a fifth layer was added to get the same layer structure at the top and bottom of the slab. The slab geometry is shown in Fig. 4. Slabs were fully relaxed allowing the three top layers to move while the two at the bottom were kept fixed at the bulk lattice constant. Surface energy was calculated according to the following formulation:

$$\theta = \frac{1}{A}[E_{slab} - nE_{Bulk}] \quad (1)$$

where θ is the Surface Energy, E_{slab} is the total energy of the slab, E_{bulk} is the energy per unit formula of the bulk, n is the number of units formula in the slab and A is the slab surface area. We obtained negative surface energies of around −0.24 eV for the different slabs studied, with slight differences of at most 2 meV indicating that all surfaces considered may co-exist. Although this is the case, we identified the slab having the lowest surface energy as the most stable for the rest of our analysis. Interestingly, the *negative* surface energy is a result of the *low stability* of this material. For a stable solid, surface energies are always positive because the formation of a surface requires additional work. In Zn_3P_2, negative surface energies indicate that the surface is more stable than the bulk; therefore, the solid would transform spontaneously into surfaces leading to the disintegration of the compound [29]. The negative values of the surface energy are one of the many characteristics responsible of the low stability of the compound. Atomic reconstruction resulting from the recombination of the surface dangling bonds is reported in Fig. 4, where the atomic displacements in the *x*, *y*, and *z* directions are represented. As mentioned above, each slab layer is composed of 6 Zn and 4 P atoms, therefore in Fig. 4d the *x* axis represents all atoms forming the surface (1st layer) and subsurface layer (2nd layer).

From Fig. 4d it is observed that the largest displacements of Zn atoms are in the *z* and *y* directions, while those in the *x* direction are almost negligible. Most of the Zn atoms move from the surface downwards while P atoms move upwards. Zn and P atoms in the second layer have very minor displacements, and those in the third layer have completely negligible displacements.

The electronic structure of the slab is modified by the surface reconstructions. Fig. S1 of Supplementary Information depicts the DOS of the reconstructed surface, with contributions from the surface (1st layer) and the last layer. The DOS is very similar to that found for the bulk; however some new states are found close to the beginning of the valence band which has the effect of reducing the bang gap. These new states come from the artificial dangling bonds present at the bottom layer in the finite slab.

DFT analysis of adsorption of 4-ATP and 1,3-PDT on Zn_3P_2 surface

Functionalization of Zn_3P_2 nanowire surfaces was realized experimentally with 4-ATP [11]. This molecule has an SH termination, and once the molecule is adsorbed, its S–H bond breaks and S forms a new bond with a Zn surface atom. Molecular adsorption is possible on different surface sites represented in Fig. 5. We performed electronic structure calculations on 4-ATP adsorbed on different sites in order to compare the stability of the adsorbed molecule. For

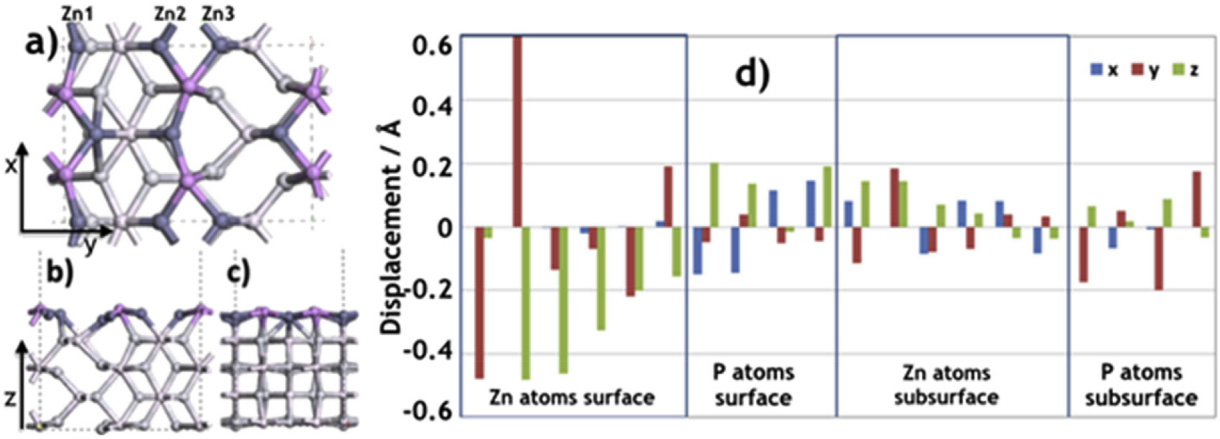

Fig. 4 – Different views of the Zn_3P_2 (100) surface after surface relaxation: a) top view, b) and c) side views. d) Atomic displacements (in Å) of topmost Zn and P surface atoms and those of the second layer in the x (blue), y (red) and z (green) directions respectively are shown by bars. The x axis represents all atoms forming the surface (1st layer) and subsurface layer (2nd layer) respectively in each box. Zn_1, Zn_2 and Zn_3 are labeled because they suffer noticeable displacements. (For interpretation of the references to color in this figure legend, the reader is referred to the web version of this article.)

comparison, we also performed electronic structure calculations on 1,3-PDT molecules adsorbed at different sites of the Zn_3P_2 surface.

Several adsorption sites were tested, starting with top sites, but the molecule preferred bridge sites. For bridge sites the S atom was initially set in the mid-way between two Zn atoms and was allowed to relax. Sites marked as x and y gave similar adsorption strengths than the B3 site.

The adsorption energy for 4-ATP is similar for all sites, except for the T2 site, the adsorption strengths are between −1.0 and −1.7 eV (Tables 2a and 2b). Differences in adsorption energy are related to the specific site and surface restructuring. The preferred optimized adsorption site for 4-ATP is very similar whether the initial position is top or bridge, in both cases the S atom of 4-ATP is bonded to a single Zn surface atom. Even when the initial position for the bridge site was at the same distance from two Zn atoms of the surface, the molecule separates from one of the Zn surface sites and gets closer to the other Zn atom. Table 2b shows that bridge sites 1, 4, and 2 have very similar adsorption energies; 4 and 2 are bonded to two Zn atoms; however the strongest site is that where S is bonded to a single Zn atom. All adsorption energies were calculated with PBE XC-functional. To test the effect of an improved theoretical description, adsorption energies were recalculated based on single point calculations using HSE06. These energies resulted approximately ~0.2 eV stronger than, but keeping the trends of the calculations obtained using PBE.

From the electronic density isosurface graphs (Fig. 6b′) it can be seen that there is shared electronic density between Zn and only one S atom. For adsorption on top sites, surface reconstruction caused by the presence of the adsorbates is shown to be higher than that when the molecule is adsorbed

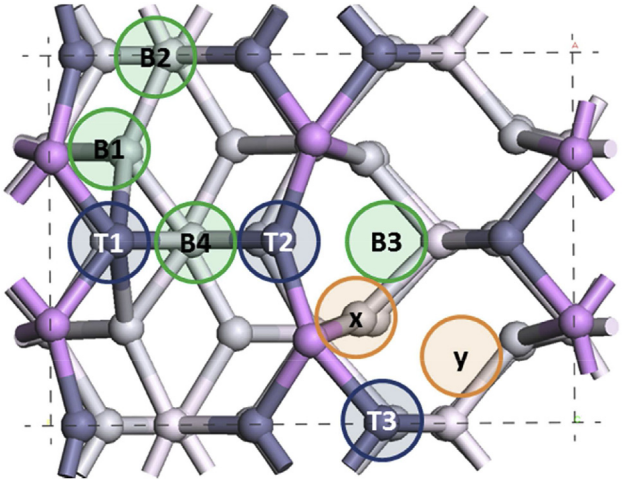

Fig. 5 – Initial adsorption sites on the Zn_3P_2 surface, only first layer atoms are colored: Zn (gray) and P (pink), bottom layers are depicted in white. Blue circles are top sites (T), green are bridge (B) and orange sites are x and y sites that gave similar adsorption strengths than bridge 3 (see text). Dotted lines denote the unit cell limits. (For interpretation of the references to color in this figure legend, the reader is referred to the web version of this article.)

Table 2a – Energetic and geometric parameters of the adsorption of 4-ATP in Zn_3P_2 *initially in top position* (values in red are distances and angles with respect to the closest P atom if present). Highlighted row represents the highest adsorption site represented in Fig. 6a.

	E_{ads}/ eV (PBE)	$d_{S\text{-}Zn}$ / Å	Zn-S-C angle /°
T1	-1.431	2.227	109
T2	0.013	2.411	134
T3	-1.401	2.432	110
		2.178	117

Table 2b – Energetic and geometric parameters of the adsorption of 4-ATP in Zn_3P_2 *initially in bridge position*. Highlighted row corresponds to the highest adsorption site represented in Fig. 6b.

	E_{ads}/ eV (PBE)	$d_{S\text{-}Zn}$ / Å	Zn-S-C angle/°
B1	-1.707	2.507	122
B2	-1.400	2.317	110
		2.421	124
B3	-1.062	2.271	116
B4	-1.683	2.272	118
		2.387	112
B5	-0.946	2.509	120
		2.207	103

Table 2c – Energetic and geometric parameters of the adsorption of 1,3-PDT in Zn_3P_2 in bridge sites. Highlighted row corresponds to the highest adsorption site represented in Fig. 6c.

	E_{ads}/ eV (PBE)	$d_{S\text{-}Zn}$ / Å	Zn-S-C angle /°
B1	-1.311	2.421	116
		2.142	112
B2	-2.376	2.465	107
		2.258	109
B3	-1.460	2.279	114
B4	-2.093	2.439	108
		2.295	112

on Bridge sites. The reconstruction not only affects the atom over which the adsorption occurs but also other Zn and P atoms that move away from the molecule. The electronic density isosurface (Fig 6a′) shows no bonding of S to other atoms. For the 1,3-PDT molecule the adsorption is stronger in bridge sites (Table 2c); the optimization led to similar distances and angles as in the case of 4-ATP with both Zn atoms inducing a high level of surface reconstruction. The isosurface densities in this case (Fig. 6c′) show electronic density shared by two Zn atoms. When the S atoms of organic molecules get closer to a P atom, no bond is formed as no electronic density is shared among them, (Fig. S2) depicts electronic density analysis between P and S atoms.

Comparison of the adsorption energies of 1,3-PDT and 4-ATP demonstrates clearly that the chemisorption on 1,3-PDT, B2 sites is stronger and leading to higher stability and better functional coating as found in the experimental results shown below. The shorter interatomic bonds support this further. This also favors a higher charge transfer from the molecule to the surface seen in the next section.

Electronic structure changes due to adsorption

Changes in electronic structure are analyzed in terms of Bader charge of individual atoms. This analysis was done before and after adsorption. Table 3 displays the calculated values. Charge of atoms on the surface as well as the charge of

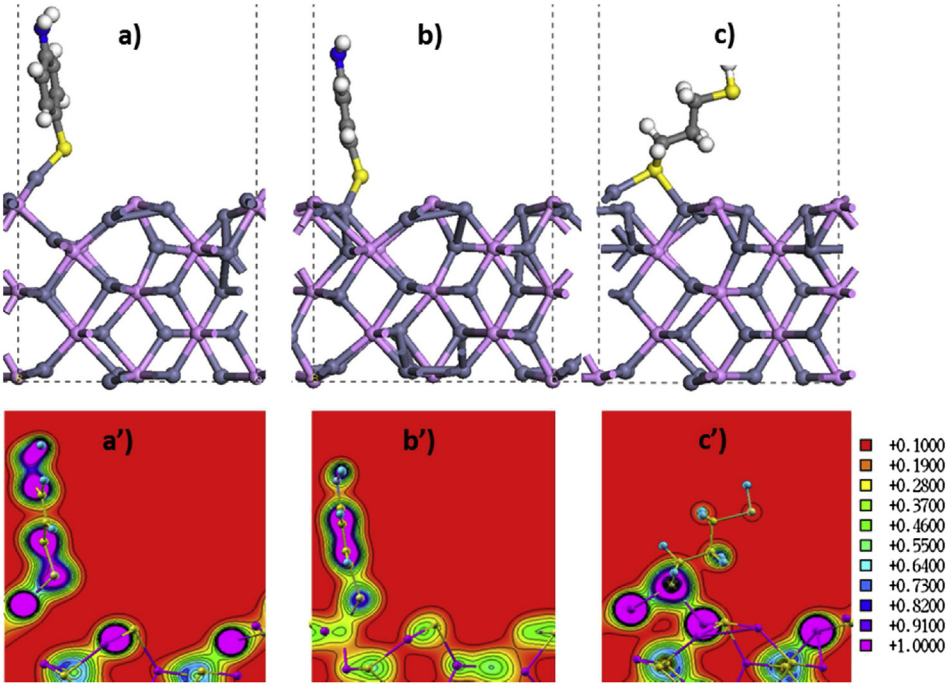

Fig. 6 – Side view of the strongest adsorption sites of 4-ATP a) Top, b) Bridge and c) 1,3-PDT bridge site. Background blue and pink atoms represent atomic positions of the surface before adsorption. a′), b′), c′) Electronic density isosurfaces with the scale shown at right. (For interpretation of the references to color in this figure legend, the reader is referred to the web version of this article.)

Table 3 – Bader charge of surface atoms and organic molecule before and after adsorption, shaded values are those atoms that bond directly to organic molecules.

Reacting atoms	Before adsorption	Surface + 1,3-PDT	Surface + 4-ATP-Top	Surface + 4-ATP-Bridge
Zn1	+0.55	0.71	0.70	0.63
Zn2	+0.58	0.68	0.60	0.59
Zn3	+0.59	0.57	0.54	0.59
Zn4	+0.61	0.54	0.53	0.55
Zn5	+0.58	0.59	0.58	0.63
Zn6	+0.53	0.55	0.54	0.57
P7	-0.84	-0.80	-0.80	-0.79
P8	-0.81	-0.87	-0.87	-0.76
P9	-0.84	-0.82	-0.80	-0.81
P10	-0.83	-0.88	-0.85	-0.84
S	-0.05/-0.09	-0.42	-0.32	-0.25
S/N directed to surface	-0.06/-1.32	-0.02	-1.25	-1.29
Slab		0.36	0.33	0.20
Organic		-0.36	-0.33	-0.20

bonding atom of the molecule are shown. Although atomic charges are not physical observables, and their calculated values depend on the specific method used, they are useful indicators of the electronic distribution in the system.

Before adsorption, all Zn atoms on the surface have similar positive charges, and all P atoms bear similar negative charges. After adsorption, the Zn atom that is directly bonded to the molecule has the highest charge change, becoming more positive, i.e. it has donated charge. Other Zn atoms change their oxidation state slightly; however the total charge of Zn atoms becomes more positive after adsorption. P atoms have the opposite trend: two of them which are the closest to the adsorbed molecules become more negative and the other two not interacting with the adsorbed molecule become less negative. In general there is a charge transfer process from the organic molecule to the Zn_3P_2 surface; the effect is higher on the bridge adsorption of 1,3-PDT mainly because of the charge transfer to both bonded Zn atoms and because of the stronger bonding to this site. On the other hand, for 4-ATP the top position leads to higher charge transfer to the Zn atoms compared to the case involving adsorption in bridge position, which may be related to the shorter bond distance (Zn–S) in the top site in comparison to the bridge site.

Projected DOS were calculated for the organic molecules adsorbed on the different sites using the HSE-06 functional (Fig. 7). In order for the electron to be driven from the Zn_3P_2 surface to the functionalizing molecules, it is expected that localized states belonging to the lowest unoccupied molecular orbital (LUMO) of the adsorbed molecule should be found between the valence and the conduction bands. Indeed, after adsorption a small peak appears close to the middle of the band gap; this small peak arises from states resulting from the hybridization of S and Zn atoms. This is observed for 1,3-PDT adsorbed on the B3 site as well. The remaining adsorption sites do not present this feature, which is evident only in cases where the molecule interacts with just one Zn atom allowing the molecular LUMO to localize in the semiconductor bandgap (Fig. 7a). In all other sites the LUMO is so high in energy that no electron transfer is possible (Fig. 7b). Similar scenario was observed for the 1,3-PDT molecule (Fig. 8) indicating that in order to enhance the electron transfer a higher molecular coverage is needed. In the limit in which one molecule is adsorbed on each Zn

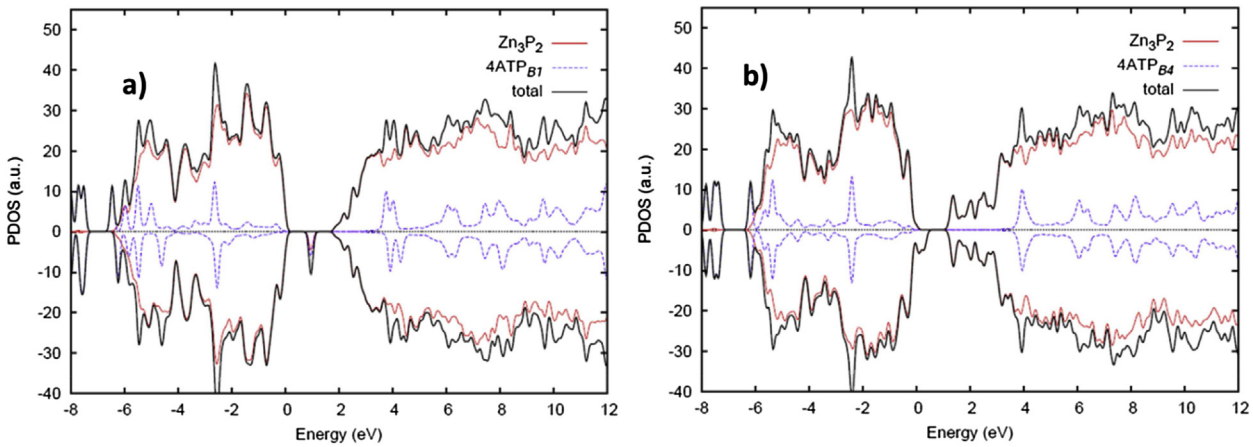

Fig. 7 – PDOS calculated with HSE-06 of 4-ATP adsorbed on a) B1 and b) B4 sites of Zn_3P_2, the contributions from semiconducting material and functionalizing molecules are depicted.

atom of the surface, a higher coverage will be also more efficient for enhancing the stability of the system against degradation.

DFT studies of charge transfer to the S atom

One of the hypotheses stated in the introduction was that functionalization of the Zn_3P_2 nanowires with organic molecules not only may improve stability but it can serve as a way to transfer electrons to a site where hydrogen production could be feasible. Considering that co-catalysts may help on this task, here we evaluate the effect a silver atom attached to the end of the organic molecule on the electronic density distribution of the complex Zn_3P_2/molecule. Fig. 9a shows a comparison of the structure and charges of the neutral system and the system with an extra electron. Even if the photochemical process cannot be simply represented by the addition of an electron this simple model reveals the change of direction of the electron flow and the possibility of electrons being transferred from the surface to the catalyst atom. Here we use Ag as a model catalyst, which would allow us to determine the main trends with respect to electron transfer when the catalyst site interacts with the coating molecule. When a single atom of Ag adsorbs on the 4-ATP and 1,3-PDT molecules the DFT study predicts the formation of a complex (Ag-4-ATP and Ag-1,3-PDT) due to the interaction of the metal site with the N atom of the molecule.

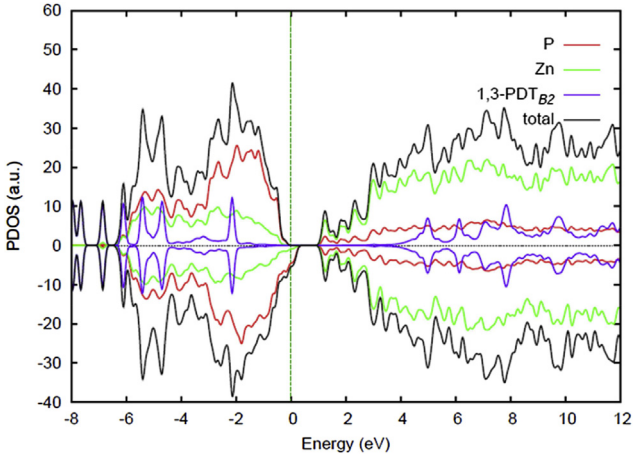

Fig. 8 – PDOS calculated with HSE-06 of 1,3-PDT adsorbed on the most stable B2 sites of Zn_3P_2, the detailed contributions from semiconducting material and functionalizing molecule are depicted.

Silver atoms are attached to the N atom of the 4-ATP molecule, the N atom arranges with the two H and the Ag atoms in tetrahedral directions. The overall geometry is not affected by the extra charge (Fig. 9b) but individual charges indicate that the extra electron preferentially locates on the Ag and S atoms, with other atoms in the surface and 4-ATP molecule remaining unaltered. Therefore, when the photochemical reaction takes place, the electron may be driven to the Ag atom passing through the 4-ATP molecule. A similar behavior is observed for the charge transfer process with 1,3-PDT; however the calculated amount of charge transfer to the Ag atom is slightly smaller (Fig. 9c).

Fig. 9c shows a comparison of the charge transfer process in the three studied systems. When the Ag atom interacts directly with the surface (Fig. 9c, set of bars at the bottom), it adsorbs closer to P atoms (2.59 Å) than to Zn atoms (2.66 Å). The direct adsorption of Ag leads to slight charge transfer from Ag to the surface atoms; however when an extra electron is added to the system, no charge transfer was observed at all, the electron remains in the semiconducting material and the Ag atom charge remains unchanged. Better charge transfer characteristics are evident in the functionalized system which in turns is beneficial for the catalytic hydrogen production as shown in the Experimental Section. The PDOS in Fig. 10 for the system Zn_3P_2/4-ATP/Ag indicates hybridization between the orbitals belonging to the coating molecule and those of the Ag atom. Moreover, a new peak appears lower in energy next to the LUMO of coating molecule indicating that the transfer of the electron to the Ag atom is also possible once the electron is located in the coating molecule.

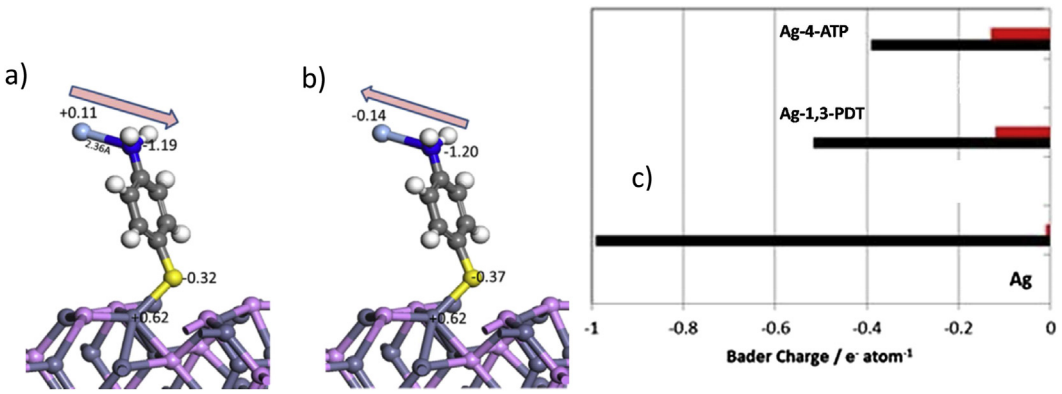

Fig. 9 – Silver atom (light blue) attached to the N terminal atom of the 4-ATP molecule. a) Neutral system and b) Charged (−1) system. Arrows show the direction of electronic density flow. c) Amount of charge transferred upon addition of an extra electron to the system. Black bars: charge remaining in the semiconducting material; red bar: charge transferred to the Ag atoms. Significant charge transfer exists when the coating molecules 4-ATP and 1,3-PDT stand between the Ag atom and the surface, while negligible charge transfer is detected in the absence of the coating molecule. (For interpretation of the references to color in this figure legend, the reader is referred to the web version of this article.)

Photocatalytic hydrogen production

The above discussion sets the basis for interpreting experiments of hydrogen production on Zn_3P_2 functionalized surfaces. Fig. 11 shows the Field Emission Scanning Electron Microscopy (FESEM) images of Zn_3P_2 nanowires functionalized with different functional groups before (a–c) and after (d–f) photocatalytic hydrogen production. Fig. 11a indicates that as-synthesized Zn_3P_2 nanowires are 50–100 nm in diameter and tens of μm in length. It can be found in Fig. 11b and c that morphologies of Zn_3P_2 nanowires were still kept after *in situ* functionalization. However, the morphologies of Zn_3P_2 transformed from nanowires to small pieces or shorter wires after photocatalytic hydrogen production except for Zn_3P_2/1,3-PDT (Fig. 11f). The transformation of morphologies could be the result from Zn_3P_2 reacting with water and forming zinc hydroxide: [11]

$$Zn_3P_2 + 6H_2O \rightarrow 3Zn(OH)_2 + 2PH_3 \quad (2)$$

Fig. 11 provides insights regarding the reasons behind the observed stabilities of the nanowires. Zn_3P_2-1,3-PDT was found to be the most stable among all the nanowire systems studied. This is believed to be due to better surface coverage of the 1,3-PDT molecules on nanowires surfaces, compared to 4-ATP, as shown in Fig. 11 b and c. Such better coverage is possible not only due to the smaller size of the 1,3-PDT molecules relative to 4-ATP, but specially because they are able to form tighter bonds with the Zn_3P_2 surfaces, as demonstrated in our computational analysis in DFT Analysis of Adsorption of 4-ATP and 1,3-PDT on Zn3P2 Surface Section. The better coverage of the nanowire surfaces with 1,3-PDT prevents any diffusion of water to the nanowire surfaces, inducing enhanced stabilities.

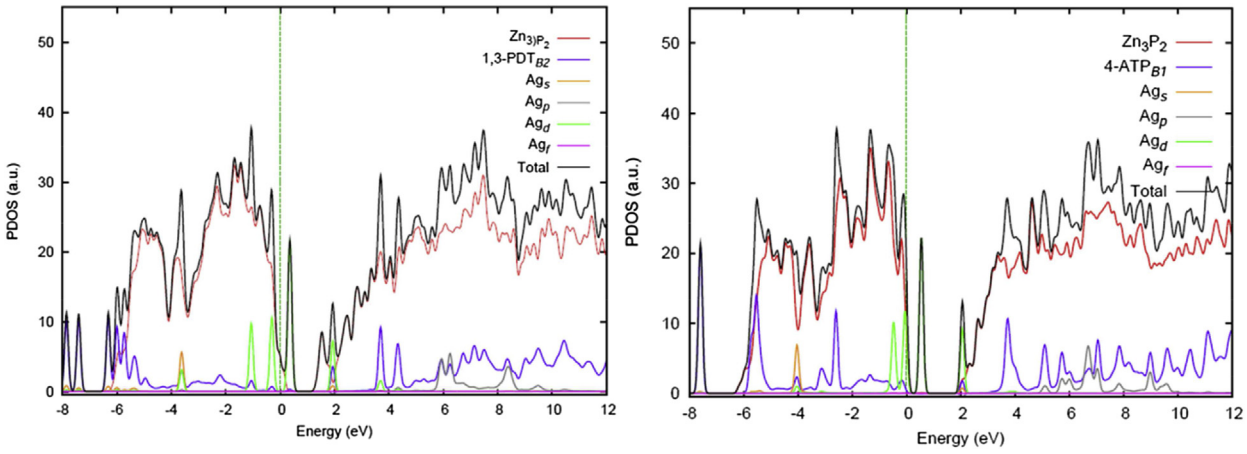

Fig. 10 – PDOS of Zn_3P_2/thiol/Ag on their strongest adsorption sites, left) 1,3-PDT on B2 right) 4-ATP on B1 site. The contribution to total DOS is shown in the legend. Near the Fermi level a hybridized state between Zn_3P_2, the thiol and the Ag appears.

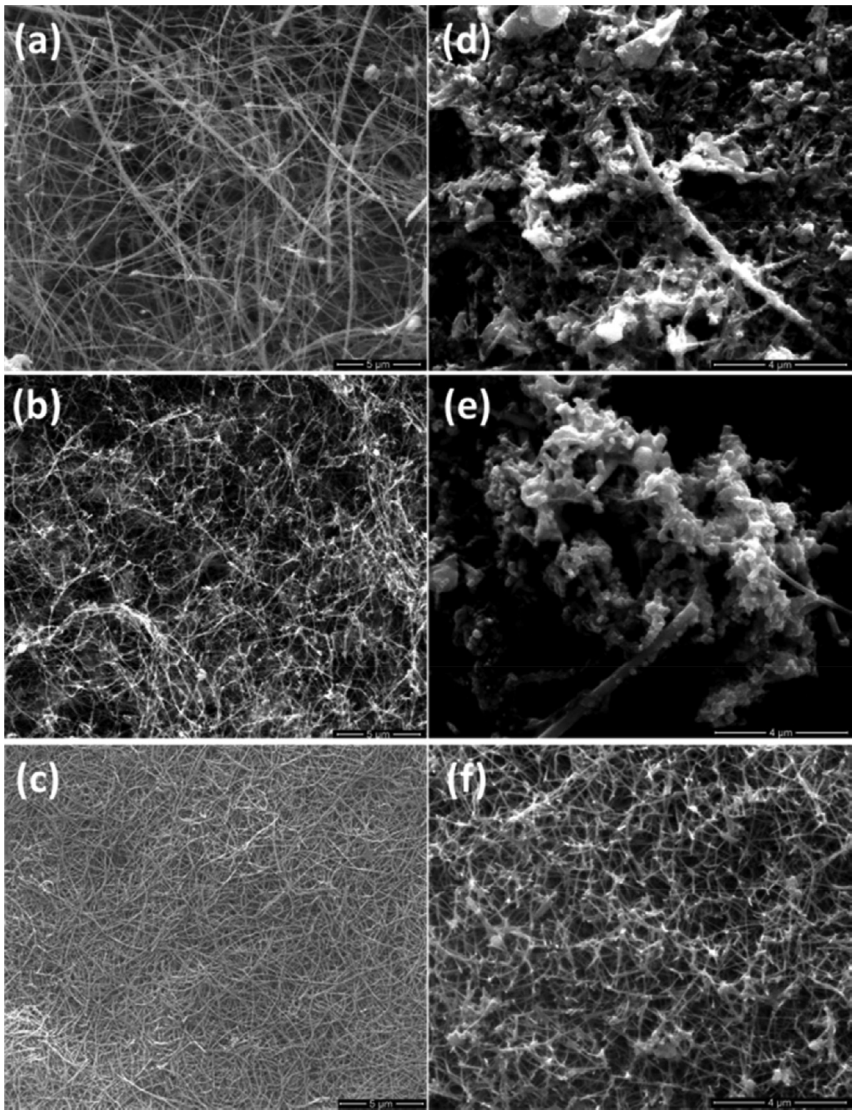

Fig. 11 – FESEM images of unfunctionalized Zn_3P_2, Zn_3P_2-4-ATP, and Zn_3P_2-1,3-PDT before (a–c) and after photocatalytic hydrogen production (d–f), respectively.

Zn_3P_2 based materials have been studied in solar cells [30,31]; however, to the best of our knowledge, it is the first time that hydrogen production was performed photocatalytically over Zn_3P_2 nanowires. Photocatalytic hydrogen production activity over Zn_3P_2 nanowires was carried out in aqueous solution containing 20 vol% of methanol acting as a hole scavenger. Fig. 12 displays time courses of photocatalytic hydrogen production from different Zn_3P_2 nanowires under visible light irradiation. In this work, pristine Zn_3P_2 nanowires and functionalized Zn_3P_2 nanowires with 4-ATP and 1,3-PDT molecules were tested. The results indicate that hydrogen production rates over pristine Zn_3P_2, Zn_3P_2/4-ATP, and Zn_3P_2/1,3-PDT are 0.03 ± 0.001, 6.52 ± 0.36, and 12.15 ± 0.34 mmol h^{-1} g^{-1}, respectively. Gentle amounts of produced hydrogen were observed in the first half hour in all tests. This could be explained as all Zn_3P_2 nanowires were undergoing the photochemical activation process [32] and further allowed hydrogen evolution at longer times. In contrast, after 4 h of irradiation, only a negligible amount of hydrogen was produced by pristine Zn_3P_2. This could be ascribed to the fact that pristine Zn_3P_2 reacts with water forming zinc hydroxide more rapidly than the two functionalized nanowires, which is consistent with eqn (2) and the FESEM image (Fig. 11d). Zn_3P_2/4-ATP showed enhanced hydrogen production that is 217 times higher than pristine Zn_3P_2 nanowires. Among the investigated samples, Zn_3P_2/1,3-PDT presents the highest hydrogen evolution rate that evolved hydrogen 405 times and nearly twice higher than that of pristine Zn_3P_2 and Zn_3P_2/4-ATP, respectively. It could be attributed to a better protection exerted by this molecular system that prevents nanowire degradation and formation of Zn hydroxide. This is in agreement with the FESEM image (Fig. 11f) illustrating that Zn_3P_2-1,3-PDT kept its morphology in spite of the oxidation environment. Functionalized Zn_3P_2 nanowires reveal hydrogen production rates comparable to those reported benchmarking visible-light responsive semiconductors [33–35] and shows

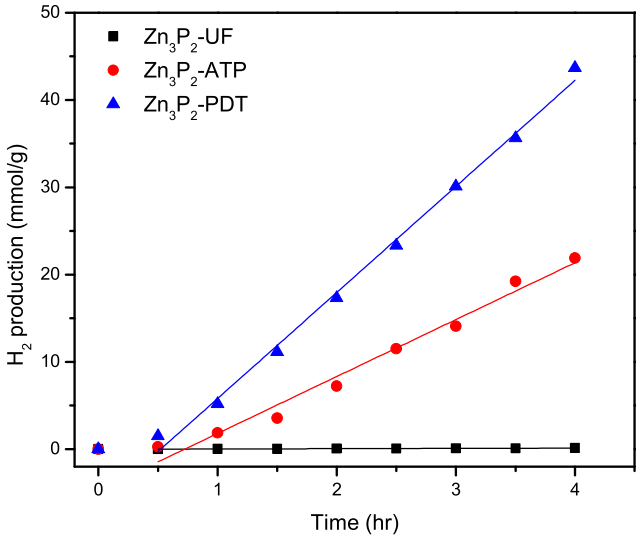

Fig. 12 – H_2 production (in mmol/gr) for Zn_3P_2 nanowires unfunctionalized (black squares), 4-ATP-functionalized (red circles), and 1,3-PDT-functionalized (blue triangles). (For interpretation of the references to color in this figure legend, the reader is referred to the web version of this article.)

the potential to keep developing this photoelectrochemical system by using earth-abundant elements.

Based on the current observations, and the known band structure of Zn_3P_2 [36], a possible H_2 formation mechanism can be formulated as follows. The absorption of light by the Zn_3P_2 nanowires leads to the formation of free electrons and holes according to the reaction: $h\nu \rightarrow h^+ + e^-$. The photogenerated holes oxidize methanol, leading to the formation of formaldehyde and hydrogen ions: $2h^+ + CH_3OH \rightarrow HCHO + 2H^+$ [37,38]. The reduction of the produced hydrogen ions by the photogenerated electrons leads to the formation of hydrogen: $2H^+ + 2e^- \rightarrow H_2$. The cathodic and anodic reactions (oxidation of methanol and the reduction of hydrogen ions respectively) are hypothesized to occur at two different locations of the nanowires. While the oxidation of methanol occurs at the surface sites on the Zn_3P_2 nanowires that are not covered with organic molecules, the reduction of hydrogen ions is expected to occur on top of the functional molecules attached to the nanowires. It is entirely possible that the nanowires have regions that are not covered with the functional molecules. This might be due to the formation of defects during the *in-situ* functionalization of Zn_3P_2 nanowires. The formation of defects during the self-assembly of monolayers is well documented [39].

As the photocatalysis reaction proceeds, the propagation of the defects in the functional molecular layer formed on top of the nanowires, leads to the availability of more number of sites for the oxidation of methanol. This in turn allows for the increased production of hydrogen (Fig. 12). Simultaneously, the degradation of the nanowires, owed to the removal of the functional molecules on the nanowires surfaces, also occurs (Fig. 11). This degradation of the nanowire morphology eventually reduces the activity of the photocatalysts. Future experimentation and computational studies will be aimed at enhancing the stability of the nanowire photocatalysts.

Conclusions

Low stability in oxidation environment has limited the application of un-functionalized Zn_3P_2 nanowires as photocatalysts. However, functionalization of Zn_3P_2 nanowires with organic molecules can improve charge transfer from bulk material to its surface as well as enhance their stability against photodegradation. Herein we find that properly surface functionalized Zn_3P_2 is a suitable photocatalyst for water–methanol mixture splitting, with hydrogen production rate as high as 12.15 mmol/h/g.

Experiments show that Zn_3P_2 coated with 1,3-PDT molecules depict better resistance to degradation than coating using 4-ATP molecules, hence providing a superior H_2 yield. Zn_3P_2 nanowires functionalized with 4-ATP and 1,3-PDT molecules greatly enhanced hydrogen evolution rates by 217 and 405 times higher than that of non-functionalized Zn_3P_2 nanowires, respectively. Using electronic structure calculations on Zn_3P_2 nanowires coated with 4-ATP and 1,3-PDT molecules we identified the most favorable adsorption sites for each molecule. Interestingly, 1,3-PDT are shown to form tighter bonds with the Zn_3P_2 surface than 4-ATP which can explain the experimentally observed degradation resistance of 1,3-PDT-Zn_3P_2. Consequently, the 1,3-PDT coating is also able to sustain H_2 production for longer times. We also showed the possibility of charge transfer from the bulk to the surface of the functionalized nanowire with and without the presence co-catalysts.

Acknowledgments

FE is grateful to the support of research computing at Texas A&M University at Qatar and for generous allocations of computer resources. GRS, MA, and PBB acknowledge computer time from Texas A&M Supercomputer Facility, Brazos HPC Cluster, and Texas Advanced Computer Center (TACC). VV and SV are grateful for financial support from NSF/DOE thermoelectrics partnership (NSF CBET #1048702).

Appendix A. Supplementary data

Supplementary data related to this article can be found at http://dx.doi.org/10.1016/j.ijhydene.2014.10.028.

REFERENCES

[1] Lewis NS. Light work with water. Nature 2001;414:589–90.
[2] Fujishima A, Honda K. Electrochemical photolysis of water at a semiconductor electrode. Nature 1972;238:37–8.
[3] Chen X, Li C, Gratzel M, Kostecki R, Mao SS. Nanomaterials for renewable energy production and storage. Chem Soc Rev 2012;41:7909–37.

[4] Komp RJ. Practical photovoltaics electricity from solar cells. Ann Arbor, Mich.: Aatec Publications; 2001.
[5] Stamov IG, Syrbu NN, Dorogan AV. Energetic band structure of Zn_3P_2 crystals. Phys B Condens Matter 2013;408:29–33.
[6] Yin W-J, Yan Y. The electronic properties of point defects in earth-abundant photovoltaic material Zn_3P_2: a hybrid functional method study. J Appl Phys 2013;113:013708–15.
[7] Fagen EA. Optical properties of Zn_3P_2. J Appl Phys 1979;50:6505–15.
[8] Wadia C, Alivisatos AP, Kammen DM. Materials availability expands the opportunity for large-scale photovoltaics deployment. Environ Sci Technol 2009;43:2072–7.
[9] Kimball GM, Bosco JP, Mueller AM, Tajdar SF, Brunschwig BS, Atwater HA, et al. Passivation of Zn_3P_2 substrates by aqueous chemical etching and air oxidation. J Appl Phys 2012;112.
[10] Vaddiraju S, Chandrasekaran H, Sunkara MK. Vapor phase synthesis of tungsten nanowires. J Am Chem Soc 2003;125:10792–3.
[11] Brockway L, Van Laer M, Kang Y, Vaddiraju S. Large-scale synthesis and in situ functionalization of Zn_3P_2 and Zn_4Sb_3 nanowire powders. Phys Chem Chem Phys 2013;15:6260–7.
[12] Alenzi N, Liao W-S, Cremer PS, Sanchez-Torres V, Wood TK, Ehlig-Economides C, et al. Photoelectrochemical hydrogen production from water/methanol decomposition using Ag/TiO_2 nanocomposite thin films. Int J Hydrogen Energy 2010;35:11768–75.
[13] Galinska A, Walendziewski AG. Photocatalytic water splitting over Pt-TiO_2 in the presence of Sacrificial Reagents. Energy Fuels 2005;19:1143–7.
[14] Kresse G, Hafner J. Ab initio molecular dynamics of liquid metals. Phys Rev B Condens Matter Mater Phys 1993;47:558–61.
[15] Kresse G, Furthmueller J. Efficient iterative schemes for ab initio total-energy calculations using a plane-wave basis set. Phys Rev B Condens Matter 1996;54:11169–86.
[16] Perdew JP, Wang Y. Accurate and simple analytic representation of the electron-gas correlation energy. Phys Rev B 1992;45:13244–9.
[17] Heyd J, Scuseria GE. Efficient hybrid density functional calculations in solids: assessment of the Heyd-Scuseria-Ernzerhof screened Coulomb hybrid functional. J Chem Phys 2004;121:1187–92.
[18] Heyd J, Scuseria GE, Ernzerhof M. Hybrid functionals based on a screened Coulomb potential. J Chem Phys 2003;118:8207–15.
[19] Blochl PE. Projector augmented-wave method. Phys Rev B 1994;50:17953–79.
[20] Kresse G, Joubert D. From ultrasoft pseudopotentials to the projector augmented-wave method. Phys Rev B 1999;59:1758–75.
[21] Monkhorst HJ, Pack JD. Special points for Brillouin-zone integrations. Phys Rev B 1976;13:5188–92.
[22] Frisch MJ, Trucks GW, Schlegel HB, Scuseria GE, Robb MA, Cheeseman JR, et al. Wallingford CT; 2009.
[23] Kudin KN, Scuseria GE. Linear-scaling density-functional theory with Gaussian orbitals and periodic boundary conditions: efficient evaluation of energy and forces via the fast multipole method. Phys Rev B Condens Matter Mater Phys 2000;61:16440–53.
[24] Yazyev OV, Kudin KN, Scuseria GE. Efficient algorithm for band connectivity resolution. Phys Rev B 2002;65:205117–8.
[25] Weigend F, Ahlrichs R. Balanced basis sets of split valence, triple zeta valence and quadruple zeta valence quality for H to Rn: design and assessment of accuracy. Phys Chem Chem Phys 2005;7:3297–305.
[26] El-Mellouhi F, Brothers EN, Lucero MJ, Scuseria GE. Modeling of the cubic and antiferrodistortive phases of $SrTiO_3$ with screened hybrid density functional theory. Phys Rev B Condens Matter Mater Phys 2011;84:115122–212.
[27] Zanin IE, Aleinikova KB, Afanasiev MM, Antipin MY. Structure of Zn_3P_2. J Struct Chem 2004;45:844–8.
[28] Zanin IE, Aleinikova KB, Antipin MY, Afanas'ev MM. Analysis of chemical bonding in Zn_3P_2 crystals from X-ray diffraction data. Crystallogr Rep 2004;49:579–84.
[29] Lodziana Z, Topsoe N-Y, Norskov JK. A negative surface energy for alumina. Nat Mater 2004;3:289–93.
[30] Yang R, Chueh Y-L, Morber JR, Snyder R, Chou L-J, Wang ZL. Single-crystalline branched zinc phosphide nanostructures: synthesis, properties, and optoelectronic devices. Nano Lett 2007;7:269–75.
[31] Luber EJ, Mobarok MH, Buriak JM. Solution-processed zinc phosphide (a-Zn_3P_2) colloidal semiconducting nanocrystals for thin film photovoltaic applications. ACS Nano 2013;7:8136–46.
[32] Yu TH, Cheng WY, Chao KJ, Lu SY. $ZnFe_2O_4$ decorated CdS nanorods as a highly efficient, visible light responsive, photochemically stable, magnetically recyclable photocatalyst for hydrogen generation. Nanoscale 2013;5:7356–60.
[33] Jang JS, Joshi UA, Lee JS. Solvothermal synthesis of CdS nanowires for photocatalytic hydrogen and electricity production. J Phys Chem C 2007;111:13280–7.
[34] Li Q, Guo B, Yu J, Ran J, Zhang B, Yan H, et al. Highly efficient visible-light-driven photocatalytic hydrogen production of CdS-cluster-decorated graphene nanosheets. J Am Chem Soc 2011;133:10878–84.
[35] Li Y, Hu Y, Peng S, Lu G, Li S. Synthesis of CdS nanorods by an ethylenediamine assisted hydrothermal method for photocatalytic hydrogen evolution. J Phys Chem C 2009;113:9352–8.
[36] Nayar PS. Properties of zinc phosphide/zinc oxide heterojunctions. J Appl Phys 1982;53:1069–75.
[37] Lu X, Xie S, Yang H, Tong Y, Ji H. Photoelectrochemical hydrogen production from biomass derivatives and water. Chem Soc Rev 2014. http://dx.doi.org/10.1039/C3CS60392J.
[38] Burstein GT, Barnett CJ, Kucernak AR, Williams KR. Aspects of the anodic oxidation of methanol. Catal Today 1997;38:425–37.
[39] Love JC, Estroff LA, Kriebel JK, Nuzzo RG, Whitesides GM. Self-assembled monolayers of thiolates on metals as a form of nanotechnology. Chem Rev 2005;105:1103–70.